chemosensors

MDPI

Article

A Portable Smartphone-Assisted Fluorescence Sensing Platform Based on Molecularly Imprinted Lanthanide MOF for Rapid Determination of Thiamethoxam in Vegetables

Run Gao [1], Li Zhao [2], Lin Ma [2], Yinan Chen [1], Jialuo Mao [1], Xiuxiu Wu [1], Jinsong Yu [1] and Hui Cao [1,*]

[1] Shanghai Engineering Research Center for Food Rapid Detection, School of Health Science and Engineering, University of Shanghai for Science and Technology, No. 516, Jungong Road, P.O. Box 454, Shanghai 200093, China
[2] Shanghai Agriculture Technology Extension & Service Center, Shanghai 201103, China
* Correspondence: caohuian@126.com; Tel./Fax: +86-21-55271117

Abstract

Thiamethoxam is a widely used neonicotinoid insecticide in agriculture, and its excessive use has raised growing concerns about food safety and environmental pollution. In this study, a portable fluorescence sensing platform was developed for the rapid detection of thiamethoxam by integrating a molecularly imprinted polymer-coated lanthanide metal–organic framework (Eu/Tb-MOF@MIP) with a smartphone-based imaging system. The synthesized Eu/Tb-MOF@MIP exhibited excellent stability in aqueous media and high thermal stability up to 270 °C, attributed to the protective imprinted polymer layer. Owing to the dual recognition mechanism arising from the ligand groups of the Ln-MOF and the specific imprinted cavities, the platform also displayed excellent selectivity toward thiamethoxam, with an imprinting factor of 3.06. Under optimized conditions, the platform enabled sensitive detection of thiamethoxam over a linear range of 0.01–9 mg·L^{-1}, with a detection limit of 9.3 μg·L^{-1}. When applied to spiked vegetable samples, the method achieved recoveries of 76.0–95.3% with relative standard deviations (RSDs) of 1.24–5.12%. Mechanistic investigation revealed that the fluorescence quenching was primarily attributable to the inner filter effect (IFE) and analyte-induced excited-state quenching, with the latter likely enhanced by MIP-mediated enrichment.

Keywords: lanthanide MOF; molecular imprinted polymer; thiamethoxam; fluorescent sensing platform; quenching mechanism

1. Introduction

Thiamethoxam, a second-generation neonicotinoid insecticide, functions as a selective agonist of insect nicotinic acetylcholine receptors and is widely used in crop protection for its high potency and broad-spectrum activity [1]. However, its improper use can lead to residues in agricultural products, soil, and water, thereby threatening ecological stability and human health [2,3]. The European Union has restricted neonicotinoid use on flowering crops and established strict maximum residue limits (MRLs) as low as 0.01 μg/g [4]. Therefore, there is an urgent need for rapid and sensitive analytical methods to determine thiamethoxam.

Conventional chromatographic techniques provide accurate quantification of pesticide residues [5–7], but require expensive instruments, complex pretreatment, and trained

Check for updates

Received: 2 September 2026
Revised: 6 October 2026
Accepted: 8 October 2026
Published: 15 October 2026

Copyright: © 2026 by the authors. Licensee MDPI, Basel, Switzerland. This article is an open access article distributed under the terms and conditions of the Creative Commons Attribution (CC BY) license.

personnel, limiting their on-site application [8]. Fluorescence sensing has attracted considerable attention because of its simplicity, fast response, high sensitivity, and low cost [9,10]. Among available luminescent materials, lanthanide metal–organic frameworks (Ln-MOFs) exhibit high specific surface area, tunable structures, large Stokes shift, and long luminescence lifetimes, making them promising materials for fluorescence sensing [11–13]. Their luminescence arises from the "antenna effect," whose ligand-to-metal energy transfer can be modulated to enhance sensitivity.

Despite these advantages, the practical application of Ln-MOF-based sensors remains limited by their insufficient stability in aqueous environments. This instability primarily arises from the susceptibility of metal–ligand coordination bonds to hydrolytic attack [14]. Although strategies such as incorporating azole-based ligands (e.g., imidazole, pyrazole, triazole, and tetrazole) capable of forming strong nitrogen–metal bonds, or employing rigid/hydrophobic linkers to shield coordination sites, have been developed to improve water stability, the resulting frameworks still exhibit inadequate durability for long-term sensing applications [15]. In addition, conventional Ln-MOFs typically lack specific molecular recognition sites, as their ligands are not tailored toward particular target analytes; consequently, their selectivity remains limited, making reliable detection in complex sample matrices challenging [16].

Molecular imprinting provides an effective approach to enhance the selectivity of Ln-MOF by fabricating recognition cavities that are complementary to a specific template in size, shape, and functional groups [17]. Encapsulating a Ln-MOF core within a molecular imprinted polymer (MIP) shell integrates the intrinsic luminescence of the framework with the specific recognition capability of the imprinted layer [18]. Notably, the cross-linked siloxane shell formed through imprinted polymerization also serves as a hydrophobic and chemical barrier, protecting the Ln-O coordination bonds from direct contact with water and thereby improving the structural stability of the parent Ln-MOF [19,20]. For example, Eskandari et al. reported an MIP-capped luminescent MOF with enhanced selectivity for chlorpyrifos [21]. However, imprinting-stabilized Ln-MOF sensors with portable visual readout for neonicotinoids remain rarely reported.

Herein, we developed a portable smartphone-assisted fluorescence platform for thiamethoxam detection based on a molecularly imprinted Eu/Tb-MOF (Eu/Tb-MOF@MIP). A ligand–Tb^{3+}–Eu^{3+} sensitization pathway was employed to enhance the energy-transfer efficiency and fluorescence response. Meanwhile, a surface-imprinted siloxane shell was introduced onto the Eu/Tb-MOF to generate thiamethoxam-specific cavities and improve the hydrolytic stability of the Ln-MOF core. The sensing performance, stability, response mechanism, and applicability to vegetable samples were evaluated. This work offers a simple, cost-effective, and reliable strategy for the portable detection of thiamethoxam residues.

2. Materials and Methods

2.1. Reagents and Materials

Thiamethoxam, acetamiprid, imidacloprid, clothianidin, thiacloprid, and nitenpyram were purchased from the Shanghai Pesticide Research Institute (Shanghai, China). Europium nitrate pentahydrate (99.9%), terbium nitrate pentahydrate (99.9%), trimesic acid (H_3BTC, 98%), and N, N-dimethylformamide (DMF, 99.5%) were obtained from Aladdin Chemical Reagents Co., Ltd. (Shanghai, China). Methacrylic acid (MAA, 99%), styrene (≥99%), ethylene glycol dimethacrylate (EGDMA, 98%), γ-methacryloxypropyltrimethoxysilane (MPS, KH-570), azobisisobutyronitrile (AIBN, 99%), and vinyl-POSS (95%) were purchased from Sigma Aldrich (St. Louis, MO, USA). Other reagents were of analytical grade from Sinopharm Chemical Reagent Co., Ltd. (Shanghai, China).

2.2. Instrumentation

The absolute photoluminescence quantum yield (PLQY) of the Eu/Tb-MOF powder was measured at room temperature using an Edinburgh FLS1000 fluorescence spectrometer (Edinburgh Instruments Ltd., Livingston, UK) equipped with an integrating sphere. The solid sample was excited at 260 nm, and the PLQY was calculated by integrating the excitation-light scattering region and the emission spectrum over the 450–730 nm range. As this is an absolute method, no reference standard was required. The morphology and microstructure were characterized using an FEI Inspect F50 scanning electron microscope (SEM, Thermo Fisher Scientific, Hillsboro, OR, USA) and an FEI Tecnai F20 transmission electron microscope (TEM, Thermo Fisher Scientific, Hillsboro, OR, USA). Fourier-transform infrared spectra (FT-IR), X-ray diffraction (PXRD) patterns, and thermogravimetric analysis (TGA) curves were obtained using a PerkinElmer spectrometer (PerkinElmer Inc., Waltham, MA, USA), Bruker D2 PHASER (Bruker Corporation, Billerica, MA, USA) diffractometer, and TGA 5500 analyzer (TA Instruments, New Castle, DE, USA), respectively. Photoluminescence spectra were recorded on a Shimadzu RF-6000 spectrofluorometer (Shimadzu Co., Ltd., Kyoto, Japan). Smartphone images were captured with a Huawei smartphone equipped with a macro lens under illumination from a 255 nm UV lamp (Shanghai, China) in a specially constructed black box.

2.3. Synthesis of Eu/Tb-MOF

Eu/Tb-MOFs with Eu/Tb molar ratios of 0:100, 1:99, 5:95, 10:90, 30:70, 50:50, and 100:0 were synthesized with a fixed total lanthanide content of 0.56 mmol. For each Eu/Tb molar ratio, the corresponding amounts of $Eu(NO_3)_3{\cdot}5H_2O$, $Tb(NO_3)_3{\cdot}5H_2O$, sodium acetate (0.2 mmol), and H_3BTC (0.8 mmol) were dissolved in 24 mL of mixed solvent (8 mL water and 16 mL DMF). After ultrasonication, the resulting mixture was transferred to a Teflon-lined stainless-steel autoclave and heated at 80 °C for 24 h. The precipitate was collected by centrifugation, washed with ethanol, and vacuum-dried at 60 °C for 12 h.

2.4. Surface Vinyl Functionalization of Eu/Tb-MOF

To introduce polymerizable vinyl groups onto the MOF surface, 60 mg of Eu/Tb-MOF with a Eu/Tb ratio of 10:90 was dispersed in a water/ethanol mixture (v/v = 3:1, pH 5), followed by the addition of 200 μL γ-methacryloxypropyltrimethoxysilane (MPS, KH-570). After stirring for 10 min and nitrogen purging for 30 min, the suspension was reacted at 65 °C for 3 h. The vinyl-functionalized Eu/Tb-MOF was washed with ethanol and dried at 60 °C.

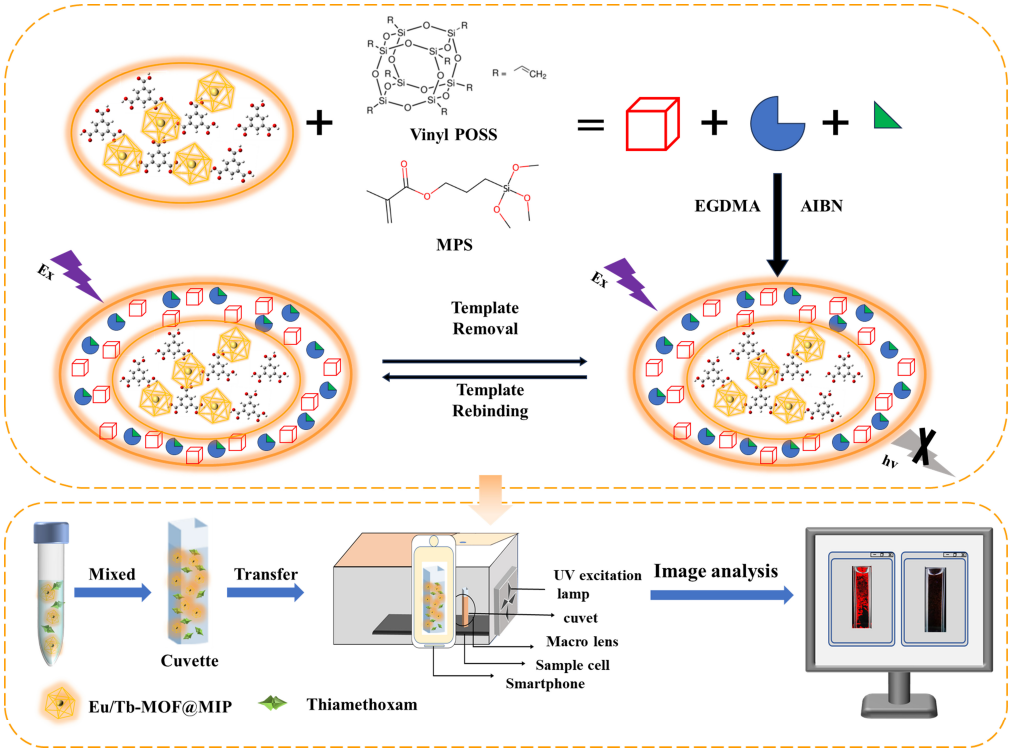
2.5. Preparation of Eu/Tb-MOF@MIP

Thiamethoxam (15 mg), methacrylic acid and styrene were dissolved in 20 mL of acetonitrile at a molar ratio of 1:4:4, followed by pre-polymerization for 3 h. Subsequently, 30 mg of vinyl-functionalized Eu/Tb-MOF, 356 μL of EGDMA, 10 mg of AIBN, and 25 mg of vinyl-POSS were added sequentially. After ultrasonication and nitrogen purging for 30 min, polymerization was conducted at 60 °C for 20 h. The templates were removed by washing repeatedly with acetonitrile/ethanol (v/v = 2:8) until no thiamethoxam absorption was detected. The product was dried at 60 °C. For comparison, Eu/Tb-MOF@NIP was prepared similarly without adding thiamethoxam.

2.6. Fabrication of the Portable Smartphone Sensing Platform and Detection Procedure

A smartphone-assisted fluorescence sensing platform was designed and assembled (Scheme 1). The system includes a dark box, a fixed quartz-cuvette holder, a 255 nm UV-LED excitation source, a cooling fan for temperature control, a macro lens for image magnification, and a smartphone for image capture. The dark box eliminates ambient-light

interference to ensure reproducible imaging, while the fixed sample-to-camera distance of 6 cm provides a standardized optical path for consistent signal acquisition.



Scheme 1. Schematic workflow of smartphone-based fluorescence imaging for quantitative detection of thiamethoxam using the Eu/Tb-MOF@MIP sensor.

For detection, 80 μL of Eu/Tb-MOF@MIP suspension (0.1 mg mL^{-1}) was mixed with 720 μL of standard solution or sample extract, followed by incubation for 5 min at room temperature. The mixture was then transferred to a 1 mL quartz cuvette and placed in the sensing platform for measurement. Under excitation at 255 nm, fluorescence images were captured using the smartphone under fixed shooting parameters. The acquired images were subsequently processed using imageJ software (v1.54f) to extract the corresponding RGB values, which were used for quantitative analysis of the fluorescence response.

2.7. Selectivity and Stability Evaluation

The selectivity of the Eu/Tb-MOF@MIP sensor was evaluated by testing five structurally related neonicotinoids (acetamiprid, imidacloprid, clothianidin, thiacloprid, and nitenpyram) at a concentration of 1.0 μg mL^{-1}, following the same analytical procedure described above. Signal stability was assessed by monitoring the sensor response to 1 μg mL^{-1} thiamethoxam continuously for 120 min.

2.8. Real Sample Preparation

Chinese cabbage, green vegetables and tomatoes were used as representative matrices for spike-and-recovery experiments. Briefly, 5 g homogenized samples, confirmed to be free of thiamethoxam, were spiked at 0, 10, 15, and 20 ng/g. After extraction with 10 mL acetonitrile/acetic acid (99:1, *v*/*v*), the samples were shaken for 3 min, treated with 6 g anhydrous $MgSO_4$ and 1 g NaCl, vortexed for 2 min, and centrifuged at 8500 rpm for 3 min. A clean-up step was further performed by transferring 9 mL of the supernatant into a 50 mL centrifuge tube containing 400 mg primary secondary amine (PSA), 400 mg graphitized carbon black (GCB), and 1200 mg octadecyl-bonded silica gel (C18). The mixture was vortexed for 5 min and centrifuged again at 8500 rpm for 3 min. Finally, 5 mL of the

supernatant was evaporated to dryness under nitrogen, redissolved in 1 mL of water, and analyzed using the Eu/Tb-MOF@MIP sensing platform (self-fabricated).

3. Results and Discussion

3.1. Luminescence Properties of Eu/Tb-MOFs

Ln-MOFs' luminescence generally originates from the "antenna effect", in which the ligand absorbs excitation energy and transfers it to the lanthanide center. However, inefficient ligand-to-metal energy transfer often leads to a low photoluminescence quantum yield, which limits sensing sensitivity. Recent studies by Xie et al. demonstrated that Tb^{3+} can serve as an energy-transfer bridge between the ligand and Eu^{3+}, which reduces energy-level mismatch, suppresses back energy transfer from Tb^{3+} and Eu^{3+} to the ligand, and minimizes non-radiative energy losses [22]. Therefore, to promote efficient energy transfer, a series of Eu/Tb-MOFs with different Eu/Tb molar ratios were synthesized under analogous hydrothermal conditions.

The excitation and emission spectra of the Eu/Tb -MOF series were recorded to elucidate their photophysical characteristics. As shown in Figure S1a–g, the excitation spectra spanned approximately 200–300 nm, with an optimum excitation wavelength at 255 nm. Under this excitation, all samples exhibited characteristic emission peaks at 545 nm (Tb^{3+}, $^5D_4 \rightarrow {}^7F_5$), 590 nm ($Eu^{3+}$, $^5D_0 \rightarrow {}^7F_1$), and 618 nm ($Eu^{3+}$, $^5D_0 \rightarrow {}^7F_2$). As the Eu^{3+} content increased from 0% to 100%, the Tb^{3+} emission at 545 nm gradually weakened, while the Eu^{3+} emission at 618 nm progressively strengthened, confirming the incorporation of both Tb^{3+} and Eu^{3+} and efficient ligand-to-metal energy transfer via the antenna effect [23]. The corresponding emission color is presented in Figure 1a,b. As the Eu/Tb ratio increased, the CIE coordinates of the samples gradually shifted from (0.3433, 0.6353) to (0.5658, 0.4146), corresponding to a visual color transition from green to bright red, consistent with the spectroscopic trends described above.

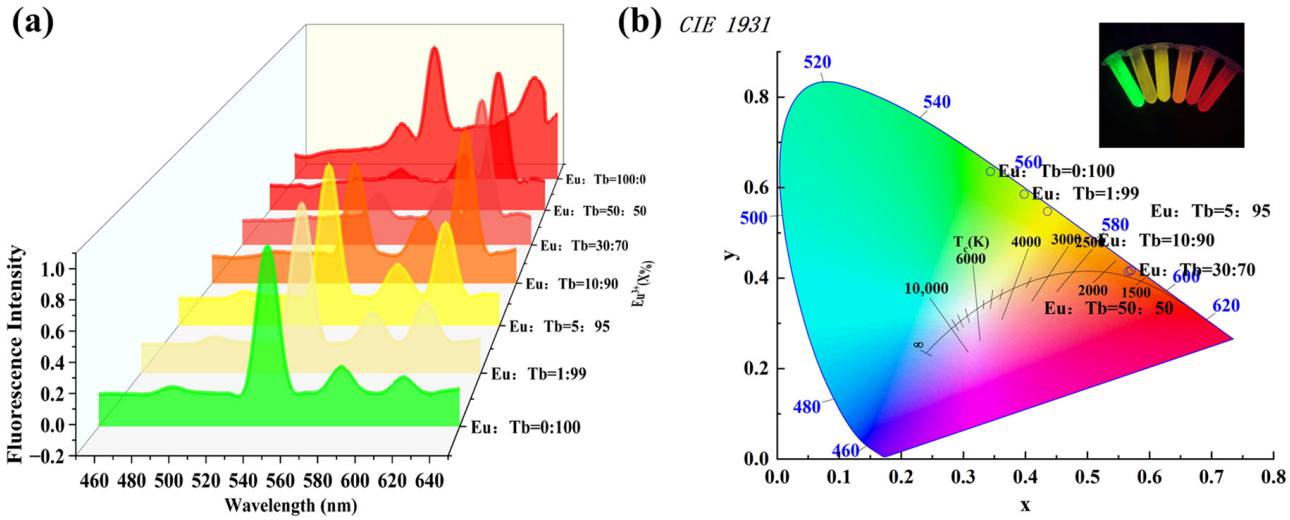


Figure 1. (**a**) Emission spectra of a series of bimetallic Eu/Tb-MOFs; (**b**) corresponding CIE chromaticity diagram of the samples.

To identify the optimal composition for sensing, the fluorescence response (R_0/R) toward thiamethoxam was investigated as a function of the Eu/Tb ratio, where R_0 and R denote the photoluminescence intensities of the Eu/Tb-MOF in the absence and presence of thiamethoxam, respectively. As illustrated in Figure S2, the Eu/Tb-MOF with a Eu/Tb ratio of 10:90 exhibited the highest response (R_0/R = 1.53) and was therefore selected for subsequent studies. Its photoluminescence quantum yield, measured using an integrating

sphere, reached 58.93% (Figure S3), which is higher than that of a previously reported Eu-MOF (42.6%) [24] and comparable to those of other mixed-lanthanide MOFs [25]. These results demonstrate the potential of the optimized Eu/Tb -MOF for high-performance fluorescent sensing.

3.2. Optimization of Eu/Tb-MOF@MIP Preparation

The Eu/Tb-MOF surface was first functionalized with MPS to introduce vinyl groups, and surface imprinting was then performed by precipitation polymerization using thiamethoxam as a template and MAA and styrene as dual functional monomers. The dual-functional monomers were chosen to complement the molecular structure of thiamethoxam: MAA can form hydrogen bonds with the nitroimino (=N-NO_2) and other nitrogen-containing heterocyclic groups of thiamethoxam [26], while styrene provides π–π stacking interactions with the thiazole ring [27]. This combination is expected to yield cavities with higher affinity and specificity than a single functional monomer. Key synthesis parameters were optimized using the quenching ratio (R_0/R) in the presence of 1 μg/mL thiamethoxam.

The effect of the template:MAA:styrene ratio was first investigated by varying the ratio from 1:2:2 to 1:8:8. As shown in Figure S4a, increasing the ratio from 1:2:2 to 1:4:4 enhanced the R_0/R value, indicating that sufficient monomer is essential for establishing non-covalent interactions with the template and generating effective recognition sites. However, a further increase to 1:8:8 resulted in a significant decrease in quenching efficiency, which was attributed to two effects. First, excess monomers favor self-polymerization in bulk solutions rather than on the MOF surface, producing non-imprinted particles that do not contribute to a specific recognition. Second, the overly thick polymer shell restricts the diffusion of thiamethoxam toward the luminescent core, thereby reducing the quenching efficiency [28]. Accordingly, a ratio of 1:4:4 was adopted for subsequent syntheses.

The monomer-to-cross-linker ratio also affected the sensing response (Figure S4b), with the maximum R_0/R value observed at a ratio of 1:9. Insufficient cross-linker resulted in a loose polymer matrix that failed to maintain the spatial geometry of the cavities after template removal, leading to poor selectivity. Conversely, excessive cross-linking generated densely packed, rigid polymer networks that buried recognition sites and inhibited thiamethoxam diffusion, thereby reducing cavity accessibility [29].

The effect of the Eu/Tb-MOF carrier dosage is shown in Figure S4c. At low dosages (10–20 mg), the available MOF surface was insufficient relative to the monomer concentration, which promoted uncontrolled self-polymerization of the imprinting precursors in solution. The resulting non-grafted particles could adsorb thiamethoxam without contributing to the fluorescence signal, thus lowering the quenching efficiency. The maximum R_0/R of 1.58 was achieved at 30 mg, indicating an optimal match between the MOF surface area and the monomer concentration that favored the formation of a homogeneous, thin imprinted layer. Further increasing the dosage to 50 mg decreased the response, probably because the low monomer-to-carrier ratio caused incomplete and nonuniform coating of the MOF particles. The bare or poorly coated regions weakened the selective enrichment of thiamethoxam and impaired its mass transfer to the recognition cavities. Therefore, 30 mg of Eu/Tb-MOF was selected as the optimal dosage.

The effect of AIBN dosage is shown in Figure S4d. The R_0/R value initially increased, peaked at 10 mg, and then declined sharply. In precipitation polymerization, AIBN acts as the radical initiator and controls the initiation rate and the homogeneity of the polymer network. An insufficient amount (5 mg) slowed the polymerization and produced a thin, poorly cross-linked imprinted layer with few stable cavities and limited porosity, and hence a low binding capacity. In contrast, excessive initiator (15–20 mg) generated a

large number of radicals simultaneously [30], which accelerated chain propagation and termination, disrupted the ordered assembly of the template–monomer complex, and yielded an inhomogeneous shell with deformed or collapsed cavities. As a result, 10 mg of AIBN was adopted for subsequent experiments.

3.3. Characterization of Eu/Tb-MOF@MIP

3.3.1. Surface Morphology and Elemental Composition

The morphologies of Eu/Tb-MOF and Eu/Tb-MOF@MIP were characterized by SEM and TEM. As shown in Figure 2a,b, pristine Eu/Tb-MOF exhibited a well-defined elongated morphology with smooth surfaces and a uniform particle size, which is typical of hydrothermal crystallization. After imprinting, the particle surfaces became rougher and the average diameter increased, attributable to deposition of the MIP shell. The average MIP shell thickness was determined to be 70 ± 7 nm from TEM images, indicating a relatively uniform coating. This shell thickness is sufficient to accommodate a considerable number of recognition cavities and facilitate efficient analyte–luminescent core interaction. The elemental composition was further analyzed using EDS mapping (Figure 3a,b). The measured Tb/Eu atomic ratio agreed well with the synthetic feed ratio, indicating precise stoichiometric control over the dual-emissive-center composition. The presence of the Si signal in Eu/Tb-MOF@MIP further confirmed that the MIP layer has been successfully formed on the Eu/Tb-MOF surface.

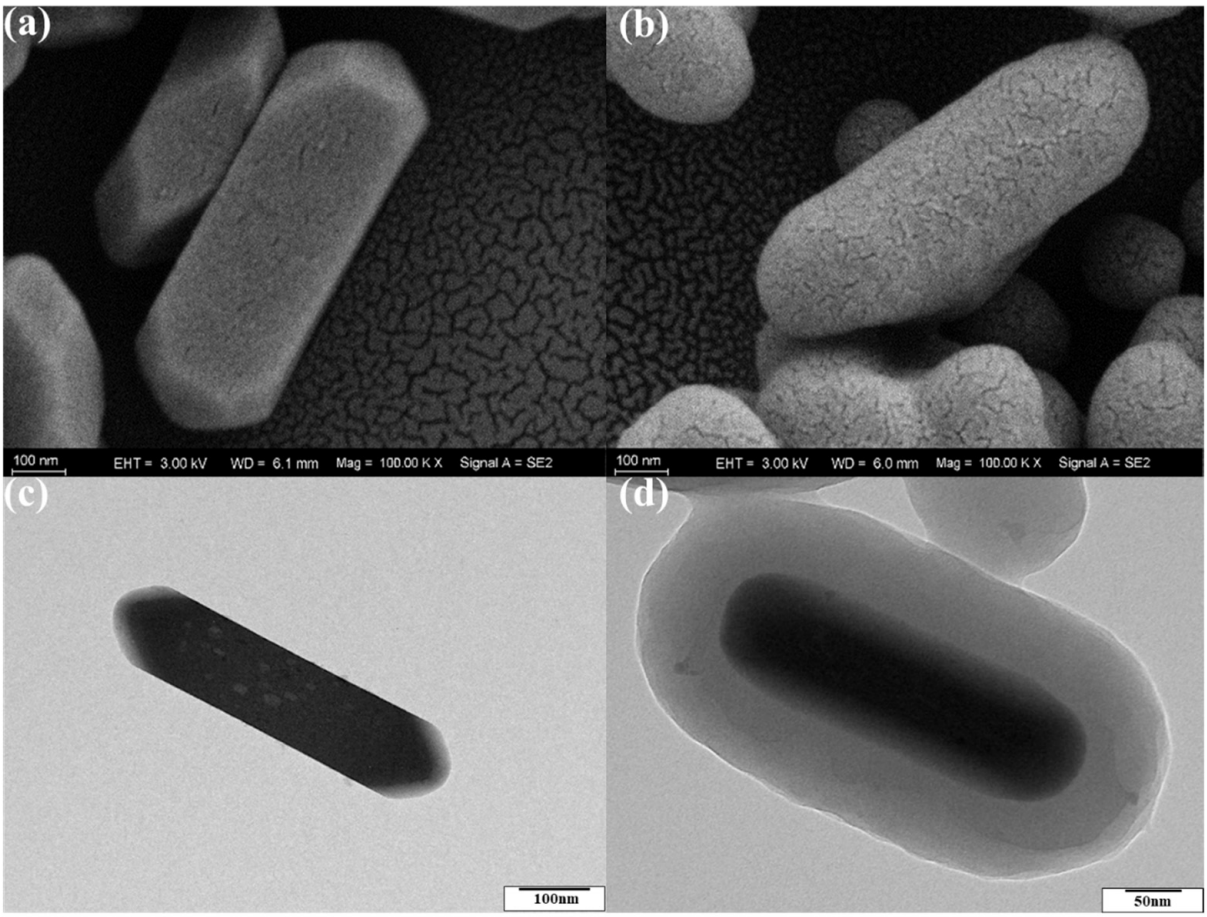


Figure 2. SEM images of (**a**) Eu/Tb-MOF and (**b**) Eu/Tb-MOF@MIP; TEM images of (**c**) Eu/Tb-MOF and (**d**) Eu/Tb-MOF@MIP.

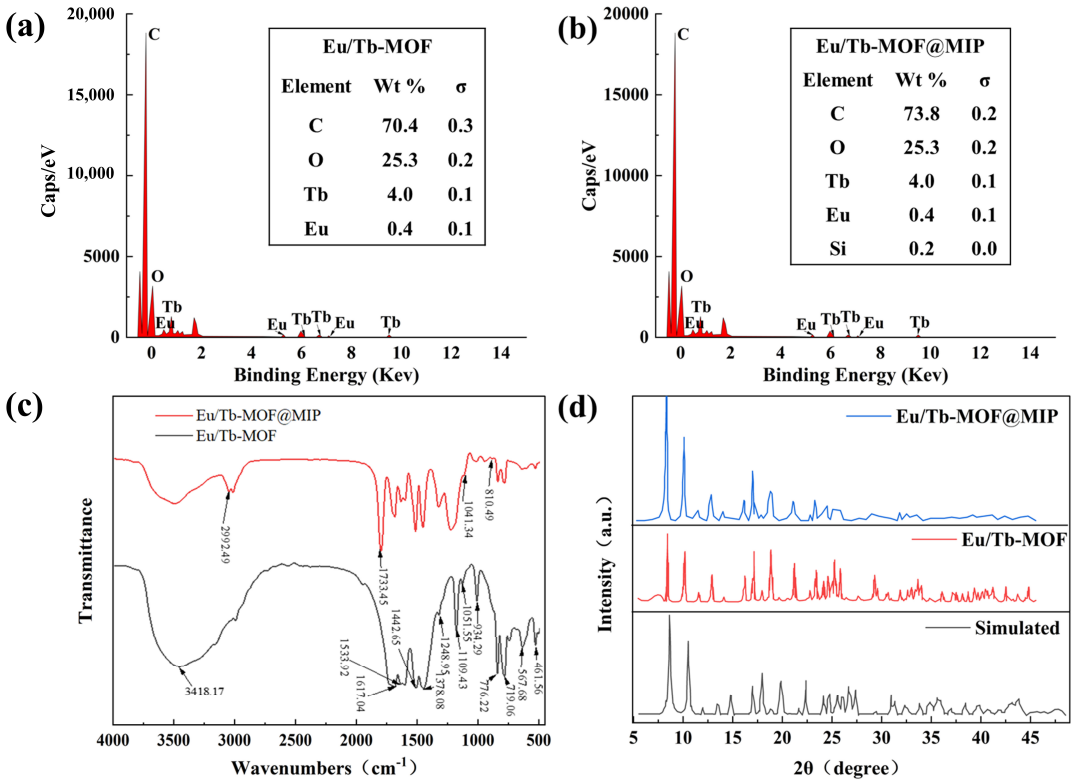


Figure 3. Characterization of Eu/Tb-MOF and Eu/Tb-MOF@MIP: (**a**,**b**) EDS spectra and elemental weight percentages; (**c**) FT-IR spectra; (**d**) experimental and simulated PXRD patterns.

3.3.2. FT-IR Analysis

The FT-IR spectra of Eu/Tb-MOF and Eu/Tb-MOF@MIP are compared in Figure 3c. For Eu/Tb-MOF, the absorption band at 3418 cm^{-1} is assigned to the –OH stretching vibration of adsorbed water. Bands in the range 1378–1617 cm^{-1} correspond to the symmetric and antisymmetric stretching vibrations of the carboxylate groups in H_3BTC; the absence of an absorption band between 1680–1800 cm^{-1} indicates the complete deprotonation of the carboxyl groups to $–COO^-$. Peaks at 924, 1051, 1109, and 1248 cm^{-1} are attributed to the in-plane bending vibrations of the benzene ring in H_3BTC, while bands at 461 and 567 cm^{-1} (Tb–O) and 719 and 776 cm^{-1} (Eu–O) confirm the coordination of both lanthanides with carboxyl groups of H_3BTC [31,32]. Following imprinting, new bands at 810 cm^{-1} and 1041 cm^{-1} (Si–O–C and O–Si–C) indicate the successful grafting of MPS onto the MOF surface [33,34]. Additionally, the band at 1733 cm^{-1} is attributed to the –C=O stretching vibration of the MAA, and the band at 2992 cm^{-1} is ascribed to the $-CH_2$ stretching vibration of the cross-linker. Collectively, these spectral features confirm the successful formation of the MIP layer.

3.3.3. PXRD Analysis

The crystalline structure was examined by PXRD. As shown in Figure 3d, Eu/Tb-MOF exhibited characteristic diffraction peaks at 8.4°, 10.1°, 12.9°, 17.2°, and 21.2°, which closely matched the simulated pattern and confirmed its high phase purity. After imprinting, all characteristic diffraction peaks were retained at the same positions, in good agreement with the pristine framework. However, a reduction in diffraction peak intensity was observed, probably due to the surface coating of amorphous MIP on the Eu/Tb-MOF, which reduces the effective scattering volume. These results demonstrate that the crystalline framework remained intact during the surface modification, imprinting, and template extraction processes, owing to the protective siloxane coupling layer.

3.3.4. Thermal Stability

Thermal stability was evaluated by TGA. As shown in Figure 4, Eu/Tb-MOF exhibited two major weight-loss stages. The first stage, with a weight loss of approximately 23.87% between about 300 and 400 °C, can be attributed to the decomposition of coordinated organic ligands and partial framework collapse. The second stage, with a weight loss of approximately 32.56% between about 400 and 600 °C, corresponds to further decomposition of the framework. For Eu/Tb-MOF@MIP, a weight loss of about 9.55% below 100 °C was due to the release of adsorbed water and residual solvent. A subsequent major weight loss of about 67.28% between 270 and 430 °C was associated with the degradation of the surface-anchored organic polymer (MIP shell) and organic constituents of the MOF. These results indicate that the imprinted layer introduces organic constituents of lower thermal resistance, slightly reducing the overall thermal stability relative to the parent Eu/Tb-MOF.

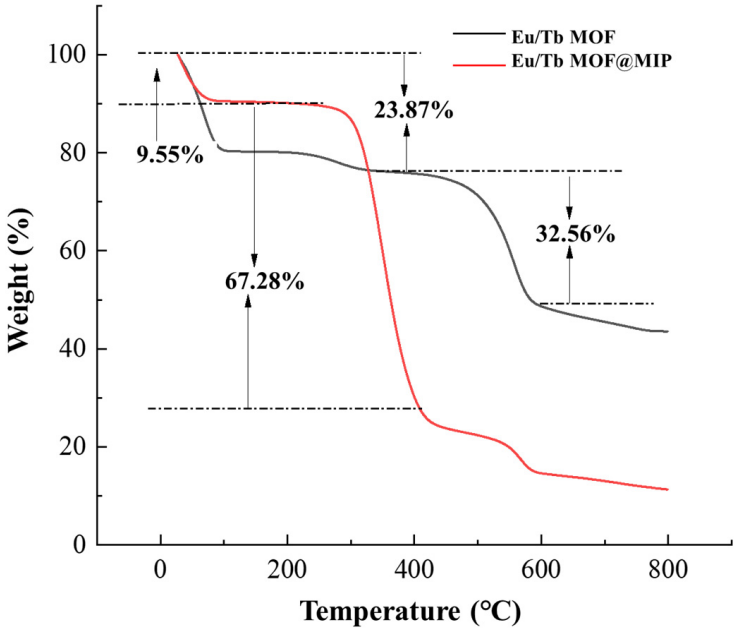


Figure 4. TGA curves of Eu/Tb-MOF and Eu/Tb-MOF@MIP.

3.4. Evaluation of Eu/Tb-MOF@MIP

3.4.1. Analytical Performance

The response of Eu/Tb-MOF@MIP toward thiamethoxam was assessed. Briefly, 80 μL of Eu/Tb-MOF@MIP suspension (0.1 mg/mL) was mixed with 720 μL of thiamethoxam standard solutions at various concentrations, and the fluorescence response was recorded following the procedure described in Section 2.6. As shown in Figure 5a, the fluorescence intensity of Eu/Tb-MOF@MIP gradually decreased with increasing thiamethoxam concentration in the range of 0.01 to 9 mg·L^{-1}, demonstrating a clear concentration-dependent quenching behavior. Based on this response, a linear calibration curve was established by plotting R_0/R against thiamethoxam concentrations, yielding the regression equation $y = 0.4056x + 1.0825$ ($R^2 = 0.9918$), which confirmed excellent linearity. The limit of detection (LOD) was calculated to be 9.3 μg·L^{-1} using the 3σ/K criterion, where σ represents the standard deviation of 12 blank measurements, and K is the slope of the calibration curve (Figure 5b). In comparison to Eu/Tb-MOF@NIP, Eu/Tb-MOF@MIP exhibited excellent selectivity for thiamethoxam with an imprinting factor of 3.06, primarily attributed to the recognition sites in the MIP layer.

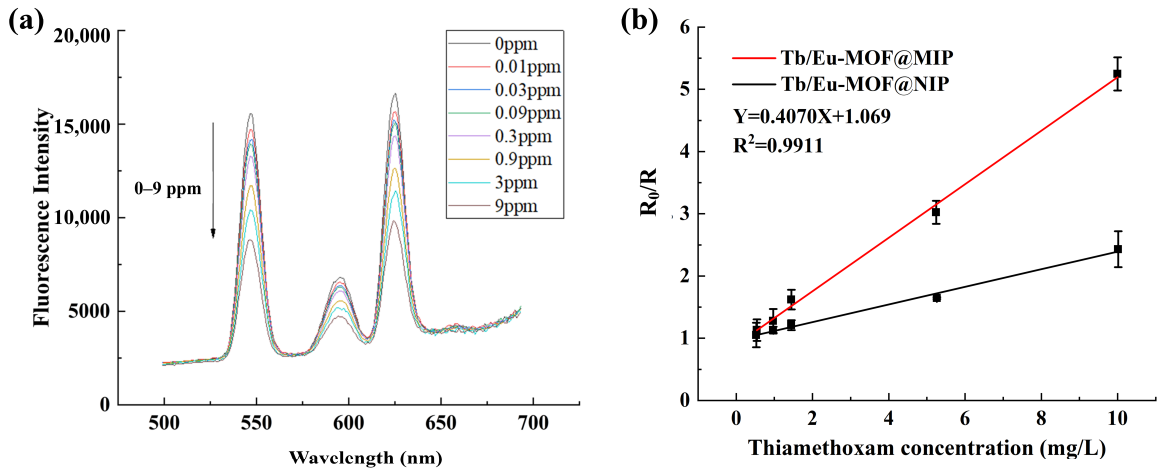


Figure 5. (**a**) Fluorescence emission spectra of Eu/Tb-MOF@MIP in the presence of increasing thiamethoxam concentrations; (**b**) linear calibration curve for thiamethoxam detection.

The performance of the Eu/Tb-MOF@MIP sensing platform for thiamethoxam analysis was further compared with previously reported methods, as summarized in Supplementary Table S1. The results reveal that the proposed Eu/Tb-MOF@MIP exhibits higher sensitivity for thiamethoxam than many of the existing methods.

3.4.2. Selectivity Evaluation

The selectivity of Eu/Tb-MOF@MIP toward thiamethoxam was evaluated against several structurally related neonicotinoid insecticides, including acetamiprid, thiacloprid, nitenpyram, imidacloprid, and clothianidin (Figure 6a). Among these analytes, thiamethoxam induced the most pronounced fluorescence quenching, while the structural analogues elicited only minor signal changes. The selective response to thiamethoxam can be attributed to the specific recognition cavities generated during molecular imprinting. The slight interference observed for the structurally similar neonicotinoids is likely associated with their structural resemblance to thiamethoxam and consequent weak, non-specific interactions with the imprinted cavities [21,35]. Compared with Eu/Tb-MOF@MIP, Eu/Tb-MOF@NIP exhibited a lower fluorescence response in the presence of all tested analytes, which was attributed to the absence of tailored recognition sites in the NIP matrix.

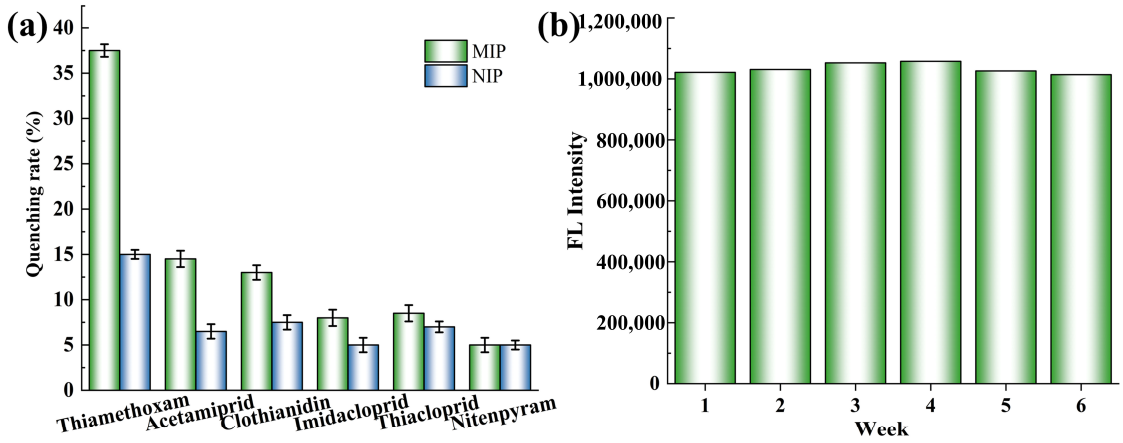


Figure 6. (**a**) Selectivity of Eu/Tb-MOF@MIP towards six neonicotinoid insecticides; (**b**) long-term storage stability of Eu/Tb-MOF@MIP.

3.4.3. Kinetics Evaluation of the Sensing Response

The kinetics of the sensing response were further examined. As shown in Figure S5, the fluorescence quenching response (R_0/R) increased rapidly after analyte addition and reached a plateau by 5 min. This rapid response can be attributed to the surface-imprinted architecture of the sensing layer, in which the shallow and easily accessible recognition cavities facilitate rapid analyte binding while avoiding the mass-transfer limitations of bulk-imprinted materials. The short equilibration time makes this sensing platform well suited for rapid on-site screening applications.

3.4.4. Stability and Reproducibility Evaluation

The signal stability of the Eu/Tb-MOF@MIP sensing platform in aqueous medium was evaluated by continuously monitoring the fluorescence response toward 1 μg mL^{-1} thiamethoxam over 120 min. As shown in Figure S6, the fluorescence response remained almost constant, demonstrating excellent signal stability. The stability of Eu/Tb-MOF@MIP in aqueous conditions was examined using fluorescence spectroscopy. As shown in Figure 6b, the fluorescence intensity remained almost constant over 6 weeks (42 days), indicating good long-term stability. This can be attributed to the protective imprinted shell surrounding the luminescent MOF core, which effectively shields the Eu^{3+}/Tb^{3+} emission centres from environmental interference and photobleaching, thereby ensuring a constant fluorescence output during long-term storage.

The effect of pH on the fluorescence response of the Eu/Tb-MOF@MIP sensor toward thiamethoxam was investigated over the pH range of 3–8, which is typical for environmental and agricultural samples. As shown in Figure S7, the R_0/R ratio exhibited only slight variation over this pH range, indicating good tolerance of the sensor to pH variation. The reproducibility of the Eu/Tb-MOF@MIP platform for thiamethoxam detection (1 μg mL^{-1}) was further assessed through batch-to-batch experiments (n = 3). As shown in Supplementary Figure S8, the Eu/Tb-MOF@MIP sensing platform has good reproducibility and is well-suited for on-site and visual detection of thiamethoxam in practical applications.

3.5. Real Sample Analysis

To evaluate the practical applicability of the proposed sensing platform, the Eu/Tb-MOF@MIP probe was applied to the determination of thiamethoxam in spiked vegetable samples, including Chinese cabbage, tomato, and leafy green vegetables, using the standard addition method. As summarized in Table 1, the recovery rates ranged from 76.0 to 95.3%, with RSDs of 1.24–5.12% (n = 3). These results demonstrate that the developed method possesses acceptable accuracy and precision, confirming its reliability for the rapid and sensitive detection of thiamethoxam residues in real food matrices.

Table 1. Recovery rates and RSDs of thiamethoxam in different spiked vegetable matrices (n = 3).

Sample	Spiked (μg/mg)	Detected (μg/mg)	Recovery (%)	RSD (%)
Chinese cabbage	1.5	1.38	92.0	4.14
	3.0	2.66	88.7	3.16
	6.0	5.71	86.2	4.21
Tomato	0.5	0.38	76.0	1.24
	1	0.82	82.0	2.31
	2	1.73	86.5	3.12
Green vegetable	1.5	1.43	95.3	5.12
	3.0	2.79	93.0	3.21
	6.0	5.71	95.2	4.21

3.6. Sensing Mechanism Analysis

3.6.1. Sensitization Mechanism of Eu/Tb-MOF

The fluorescence sensing performance of the Ln-MOFs is mainly governed by the energy transfer from the H_3BTC antenna ligand to the Tb^{3+}/Eu^{3+} centres (Figure 7a). Because of its π-conjugated aromatic structure, H_3BTC exhibits a high molar extinction coefficient and undergoes efficient π–π* transitions upon UV excitation, making it an effective sensitizer for lanthanide luminescence. Upon excitation, H_3BTC is promoted to its singlet excited state (S_1, ~32,465 cm^{-1}) and subsequently relaxes to the triplet state (T_1, ~24,786 cm^{-1}) via intersystem crossing (ISC) [36]. The S_1–T_1 energy gap is higher than 5000 cm^{-1}, which satisfies Reinhoudt's empirical criterion for efficient ISC. According to Latva's empirical rule, efficient ligand-to-lanthanide energy transfer requires the ligand triplet state (T_1) to lie approximately 2500–4500 cm^{-1} above the emitting level of the Ln^{3+} ion. However, the energy gap between the H_3BTC T_1 state and the Eu^{3+} $^5D_0$ level is large (7586 cm^{-1}), which is unfavorable for direct energy transfer and leads to incomplete sensitization [37].

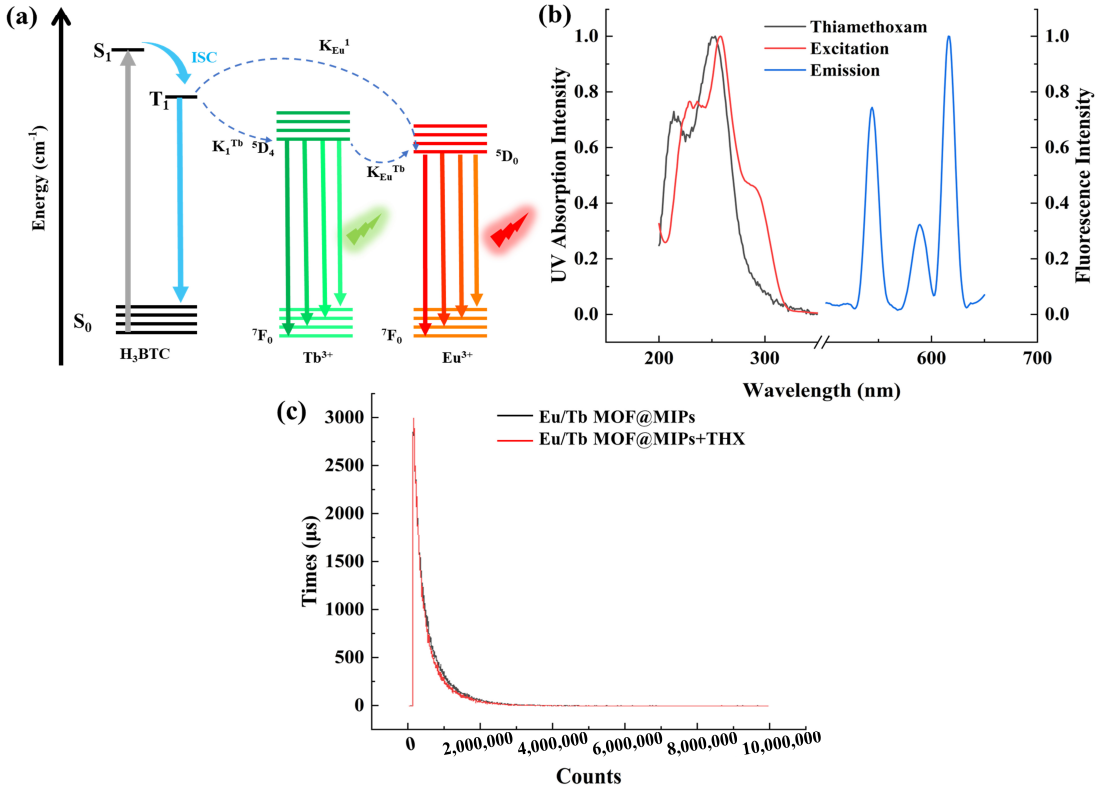


Figure 7. (**a**) Energy transfer process in Eu/Tb-MOF via the antenna effect of the H3BTC ligand. (**b**) UV absorption spectrum of thiamethoxam and excitation/emission spectra of Eu/Tb-MOF@MIP; (**c**) fluorescence lifetime decay curves of Eu/Tb-MOF@MIP with and without thiamethoxam.

The incorporation of Tb^{3+} effectively bridges this energy mismatch between the H_3BTC T_1 state and the Eu^{3+} $^5D_0$ level through its intermediate $^5D_4$ level, enabling a cascade energy transfer among $H_3BTC \rightarrow Tb^{3+} \rightarrow Eu^{3+}$. Energy transfer from the T_1 state of H_3BTC to the $^5D_4$ level of Tb^{3+} is energetically more favourable than direct transfer to Eu^{3+}, because this intermediate level reduces the effective energy gap to approximately 4286 cm^{-1}. Moreover, the presence of this intermediate Tb^{3+} level weakens undesirable back energy transfer from the excited Ln^{3+} centres to the H_3BTC triplet state, thereby reducing non-radiative losses. Subsequently, the excitation energy at the Tb^{3+} $^5D_4$ level is further transferred to the Eu^{3+} $^5D_0$ level, owing to the $5D_4$ (Tb^{3+})–$5D_0$ (Eu^{3+}) energy gap of approximately

3300 cm^{-1}, which also falls within the optimal range. This generates the characteristic red emission of Eu^{3+} and enhances the overall sensitization efficiency. Therefore, this cascade pathway helps to minimize energy mismatch, promotes stepwise energy transfer, and reduces competing back-transfer and non-radiative relaxation processes.

3.6.2. Fluorescence Quenching Mechanism

To elucidate the fluorescence quenching mechanism of Eu/Tb-MOF@MIP by thiamethoxam, several possible pathways were considered, including framework collapse, fluorescence resonance energy transfer (FRET), the inner filter effect (IFE), and dynamic or static quenching. Framework collapse was considered unlikely because thiamethoxam has limited coordination ability and cannot effectively compete with the carboxylate ligands for the lanthanide centers. FRET was also excluded because the emission spectrum of Eu/Tb-MOF@MIP showed no appreciable overlap with the absorption spectrum of thiamethoxam.

In contrast, the absorption band of thiamethoxam overlapped with the excitation spectrum of Eu/Tb-MOF@MIP (Figure 7b), indicating that the IFE contributes to the observed quenching [38]. To evaluate this contribution, the steady-state fluorescence intensities were corrected using the standard absorbance-based equation (Table S2). An evident concentration-dependent decrease in fluorescence intensity remained after IFE correction, suggesting that the observed quenching cannot be attributed solely to the IFE [39]. Furthermore, the fluorescence lifetime of Eu/Tb-MOF@MIP decreased from 470.43 to 429.98 μs after the addition of thiamethoxam (Figure 7c). Because the IFE does not change the intrinsic excited-state lifetime, this decrease indicates analyte-induced excited-state quenching.

Furthermore, the MIP shell may selectively enrich thiamethoxam near the MOF surface and the Eu^{3+}/Tb^{3+} centers, thus increasing the local analyte concentration and facilitating short-range interactions with the luminescent units. Because the emission of Eu/Tb-MOF@MIP originates from ligand-sensitized energy transfer, the bound analyte may perturb the local microenvironment, promote nonradiative deactivation of the excited ligand, or interfere with energy transfer from the ligand triplet state to Eu^{3+}/Tb^{3+}, thereby reducing the lanthanide emission [40]. Accordingly, the observed luminescence quenching is attributed to the combined contributions of the IFE and analyte-induced excited-state quenching, with the latter likely enhanced by MIP-mediated enrichment.

4. Conclusions

A portable, smartphone-assisted fluorescence sensing platform based on a molecularly imprinted Eu/Tb-MOF was developed for the rapid determination of thiamethoxam. Encapsulation of Eu/Tb-MOF particles within an MIP shell enhances both selectivity and stability by combining the molecular recognition capability of the imprinted polymer with the strong luminescence of the Ln-MOF core while protecting the coordination bonds from hydrolytic degradation. Coupled with smartphone imaging and digital analysis, the sensor enabled quantitative detection of thiamethoxam within 5 min, with a detection limit of 9.3 $\mu g \cdot L^{-1}$ and satisfactory reproducibility. Analysis of spiked vegetable samples gave acceptable recoveries and good precision. Mechanistic studies indicated that the fluorescence quenching is attributed to the combined contributions of the IFE and analyte-induced excited-state quenching, with the latter likely enhanced by MIP-mediated enrichment. The probe is currently intended for single-use detection, and the development of regenerable probes will be the focus of our future work.

Supplementary Materials: The following supporting information can be downloaded at: https://www.mdpi.com/article/10.3390/chemosensors14100232/s1, Figure S1: Excitation and emission

spectra of Eu/Tb-MOFs with different Eu:Tb molar ratios: (a) 0:100, (b) 1:99, (c) 5:95, (d) 10:90, (e) 30:70, (f) 50:50, and (g) 100:0. With increasing Eu^{3+} content, the Tb^{3+} emission at ~545 nm gradually decreases, while the Eu^{3+} emission at ~618 nm increases; Figure S2: Fluorescence response (R_0/R) of Eu/Tb-MOFs toward thiamethoxam with different Eu:Tb molar ratios. Error bars represent standard deviation (n = 3); Figure S3: Quantum yield of Eu/Tb-MOF with a Eu:Tb molar ratio of 10:90; Figure S4: Effects of (a) template-to-monomer molar ratio, (b) functional monomer-to-cross-linker molar ratio, (c) carrier dosage, and (d) AIBN dosage on the fluorescence quenching response (R_0/R) of Eu/Tb-MOF@MIP; Figure S5: Fluorescence response (R_0/R) of Eu/Tb-MOF@MIP as a function of time; Figure S6: Fluorescence response (R_0/R) stability of Eu/Tb-MOF@MIP over 120 min; Figure S7: Effect of pH (3–8) on the R_0/R response of the Eu/Tb-MOF@MIP sensing platform toward thiamethoxam; Figure S8: Reproducibility of the Eu/Tb-MOF@MIP sensing platform for thiamethoxam detection (1 mg/L), evaluated by batch-to-batch experiments (n = 5); Table S1: Comparison of thiamethoxam detection performance by different fluorescence methods; [41–46]. Table S2: Fluorescence quenching efficiency before and after IFE correction at different pesticide concentrations.

Author Contributions: R.G.: Investigation, Data curation, Validation, Writing—original draft. L.Z.: Data Curation, Editing. L.M.: Data Curation, Editing. Y.C.: Formal analysis, Methodology. J.M.: Methodology, Data curation. X.W.: Methodology, Editing. J.Y.: Methodology, Editing. H.C.: Conceptualization, Supervision, Project administration, Funding acquisition. All authors have read and agreed to the published version of the manuscript.

Funding: This project was supported by the Shanghai Agricultural Science and Technology Innovation Program (2023-02-08-00-12-F04599).

Institutional Review Board Statement: This article does not contain any studies with human participants or animals performed by any of the authors.

Informed Consent Statement: Not applicable.

Data Availability Statement: The data presented in this study are available on request from the corresponding author.

Conflicts of Interest: The authors declare that they have no known competing financial interests or personal relationships that could have appeared to influence the work reported in this paper.

References

1. Yan, W.; Zheng, Q.; Yang, L.; Zhu, S.; Zhang, Z.; Xu, H. Efficacy of Drip Irrigation with Thiamethoxam on Control of Monolepta Hieroglyphica, and Uptake, Translocation and Dietary Risk of Thiamethoxam in Maize. *Pest Manag. Sci.* **2023**, *79*, 4931–4941. [CrossRef]
2. Li, L.; Yin, S.; Kang, S.; Chen, Z.; Wang, F.; Pan, W. Comprehensive Effects of Thiamethoxam from Contaminated Soil on Lettuce Growth and Metabolism. *Environ. Pollut.* **2024**, *343*, 123186. [CrossRef]
3. Pang, N.; Fan, X.; Fantke, P.; Zhao, S.; Hu, J. Dynamics and Dietary Risk Assessment of Thiamethoxam in Wheat, Lettuce and Tomato Using Field Experiments and Computational Simulation. *Environ. Pollut.* **2020**, *256*, 113285. [CrossRef]
4. Tang, S.; Zeng, Z.; Kang, R.; Wei, Y.; Tan, G.; Chen, M.; Wang, B.; Tang, Z. Residue Analysis and Dietary Risk Assessment of 10 Neonicotinoid Insecticides in Oenanthe Javanica from Hainan Province of China. *Foods* **2024**, *14*, 78. [CrossRef]
5. Zeng, Y.; Lan, T.; Li, X.; Chen, Y.; Yang, Q.; Qu, B.; Zhang, Y.; Pan, C. A Comparison of the Determination of Multiple Pesticide Residues in Fruits, Vegetables, and Edible Fungi Using Gas Chromatography Combined with Filtration Purification and Solid-Phase Extraction. *RSC Adv.* **2024**, *14*, 16898–16911. [CrossRef]
6. Baker, S.E.; Serafim, A.B.; Morales-Agudelo, P.; Vidal, M.; Calafat, A.M.; Ospina, M. Quantification of Deet and Neonicotinoid Pesticide Biomarkers in Human Urine by Online Solid-Phase Extraction High-Performance Liquid Chromatography-Tandem Mass Spectrometry. *Anal. Bioanal. Chem.* **2018**, *411*, 669–678. [CrossRef]
7. Michlig, M.P.; Brasca, R.; Demonte, L.D.; Magni, F.V.; Repetti, M.R. Multivariate Optimization of the Extraction and Cleaning Procedure to Determine Neonicotinoids in Honey from Intensive Livestock and Agricultural Production Areas by Uhplc-Ms/Ms. *Microchem. J.* **2024**, *207*, 111672. [CrossRef]
8. Almeida, M.O.; Oloris, S.C.S.; Faria, V.H.F.; Ribeiro, M.C.M.; Cantini, D.M.; Soto-Blanco, B. Optimization of Method for Pesticide Detection in Honey by Using Liquid and Gas Chromatography Coupled with Mass Spectrometric Detection. *Foods* **2020**, *9*, 1368. [CrossRef]

9. Nie, Z.; Zhang, Z.; Yang, K.; Chen, H.; Wu, H. Research Progress on Organic Fluorescent Probes Based on Pesticide Detection. *J. Fluoresc.* **2025**, *35*, 12267–12291. [CrossRef]
10. Wu, S.y.; Zhang, X.; Tang, W.; Zhang, Y.; Lv, X.; Zhuang, Y.-T. A Ratiometric Fluorescence Platform Based on Bifunctional Mofs for Sensitive Detection of Organophosphorus Pesticides. *J. Food Compos. Anal.* **2025**, *137*, 106971. [CrossRef]
11. Xu, X.; Ma, M.; Sun, T.; Zhao, X.; Zhang, L. Luminescent Guests Encapsulated in Metal–Organic Frameworks for Portable Fluorescence Sensor and Visual Detection Applications: A Review. *Biosensors* **2023**, *13*, 435. [CrossRef]
12. Zhang, Z.; Guo, D.; Zhang, J.; Ji, C.; Yu, H.; Yang, X. Evolution of High Specific Surface Area Lanthanum Aerogels to Magnetic Lanthanum Hydroxide Nanostructures. *Inorg. Chem. Commun.* **2020**, *114*, 107818. [CrossRef]
13. Liu, N.; Zhang, Y.; Jin, S.-y.; Li, T.-t.; Dai, H.; Li, W.-y.; Xu, W. Dual-Emission Lanthanide Metal-Organic Framework as a Luminescence Sensor for Nitrofuran Antibiotics and Pesticide Detection. *Inorganica Chim. Acta* **2024**, *564*, 121958. [CrossRef]
14. Liu, C.-P.; Lin, T.-E.; Chiang, J.-C.; Chen, B.-J.; Chien, P.-H.; Chien, S.-Y.; Lee, G.-H.; Liu, Y.-H.; Lu, K.-L. An Exceptional Water Stable Terbium-Based Metal–Organic Framework for Selective Detection of Pesticides. *RSC Adv.* **2024**, *14*, 35220–35226. [CrossRef]
15. Li, J.; He, Y.; Wang, L.; Li, G.; Zou, Y.; Yan, Y.; Li, D.; Shi, X.; Song, Z.; Shi, X. Construction of Fluorescence Active Mofs with Symmetrical and Conformationally Rigid N-2-Aryl-Triazole Ligands. *RSC Adv.* **2020**, *10*, 41921–41925. [CrossRef]
16. Zhao, Z.; Yang, S.; Zhu, M.; Zhang, Y.; Sun, Y.; Wu, S. A Multicenter Lanthanide Coordination Polymer for Ratiometric Pesticide Monitoring. *Sens. Actuators B Chem.* **2023**, *383*, 133593. [CrossRef]
17. Zhang, Y.; Jin, S.; Liu, R.; Liu, Z.; Gong, L.; Zhang, L.; Zhao, T.; Chen, S.; Niu, L.; Fa, H.; et al. A New Portable Electrochemical Detection Sensor Based on Molecularly Imprinted Polymer-Modified Mof-808/Ab for the Highly Sensitive and Selective Determination of Dimethoate. *Microchem. J.* **2024**, *206*, 111436. [CrossRef]
18. Zhong, Y.; Li, Z.; Zhang, A.; Peng, Y.; Zhou, H.; Wang, B.; Xie, L.; Guo, Y. A Molecularly Imprinted Electrochemical Sensor Mip/Cu-Mof/Rgo/Aunps/Gce for Highly Sensitive Detection of Electroneutral Organophosphorus Pesticide Residues. *Microchim. Acta* **2024**, *191*, 338. [CrossRef]
19. Ma, F.; Yan, M.; Lin, R.; Wu, Y.; Pan, J. Boronate-Affinity Sol–Gel-Imprinted Membranes with Mofs-Functionalized Rotary-Evaporating Layers for High-Precision Specific Recognition. *Sep. Purif. Technol.* **2024**, *330*, 125458. [CrossRef]
20. Bai, L.; Ye, T.; Si, W.; Yu, J.; Yuan, M.; Cao, H.; Hao, L.; Wu, X.; Yin, F.; Luo, X.; et al. Molecular Imprinted Polymer Capped Luminescent Metal -Organic Framework for the Determination of Pyrethroids and Its Metabolite. *Microchem. J.* **2023**, *193*, 109047. [CrossRef]
21. Eskandari, H.; Amirzehni, M.; Hassanzadeh, J.; Vahid, B. Mesoporous Mip-Capped Luminescent Mof as Specific and Sensitive Analytical Probe: Application for Chlorpyrifos. *Microchim. Acta* **2020**, *187*, 0026–3672. [CrossRef]
22. Xie, F.; Shen, C.; Li, X.; Xiao, P.; Wang, S.; Li, Y.; Sun, H.; Wang, P.; Li, Y.; Liu, Q. An Electrochemiluminescence Sensor Based on Lanthanide Bimetallic Mofs with a "Cascade Sensitization Mechanism" for the Sensitive Detection of Ca242. *Talanta* **2024**, *273*, 125956. [CrossRef]
23. Rezende Souza, E.; Silva, I.G.N.; Teotonio, E.E.S.; Felinto, M.C.F.C.; Brito, H.F. Optical Properties of Red, Green and Blue Emitting Rare Earth Benzenetricarboxylate Compounds. *J. Lumin.* **2010**, *130*, 283–291. [CrossRef]
24. Zhang, N.; Zhang, R.; Fu, R.; Song, Q.; He, G.; Wang, S.; Zhang, L. Tunable High-Efficiency Eu/Tb-Mofs Enabling Ultrasensitive Ion Detection and Advanced Anti-Counterfeiting. *Dye. Pigment.* **2026**, *252*, 113804. [CrossRef]
25. Cruz-Estrada, L.E.; Villar-Gutiérrez, I.D.; Giambastiani, G.; Falcony, C.; Castillo-Blum, S.E.; Rossin, A. White Light Emission and Energy Transfer in Mixed-Metal Europium/Terbium/Thulium Formate Metal–Organic Frameworks: Effect of Lanthanum Dilution. *Adv. Opt. Mater.* **2026**, *14*, e71447. [CrossRef]
26. Silva, C.F.; Menezes, L.F.; Pereira, A.C.; Nascimento, C.S. Molecularly Imprinted Polymer (Mip) for Thiamethoxam: A Theoretical and Experimental Study. *J. Mol. Struct.* **2021**, *1231*, 129980. [CrossRef]
27. Han, X.; Kong, H.; Chen, T.; Gao, J.; Zhao, Y.; Sang, Y.; Hu, G. Effect of ΠI–ΠI Stacking Interfacial Interaction on the Properties of Graphene/Poly(Styrene-B-Isoprene-B-Styrene) Composites. *Nanomaterials* **2021**, *11*, 2158. [CrossRef]
28. Golker, K.; Nicholls, I.A. The Effect of Crosslinking Density on Molecularly Imprinted Polymer Morphology and Recognition. *Eur. Polym. J.* **2016**, *75*, 423–430. [CrossRef]
29. Che Lah, N.F.; Ahmad, A.L.; Low, S.C. Molecular Imprinted Membrane Biosensor for Pesticide Detection: Perspectives and Challenges. *Polym. Adv. Technol.* **2020**, *32*, 17–30. [CrossRef]
30. Viltres-Portales, M.; Alberto, M.D.L.; Ye, L. Synthesis of Molecularly Imprinted Polymers Using an Amidine-Functionalized Initiator for Carboxylic Acid Recognition. *React. Funct. Polym.* **2021**, *165*, 104969. [CrossRef]
31. Fang, Y.; Li, Y.; Zang, X.; Chen, Y.; Wang, X.; Wang, N.; Meng, X.; Cui, B. Gold-Copper-Doped Lanthanide Luminescent Metal-Organic Backbone Induced Self-Enhanced Molecularly Imprinted Ecl Sensors for Ultra-Sensitive Detection of Chlorpyrifos. *Food Chem.* **2024**, *443*, 138533. [CrossRef]
32. Yue, X.; Fu, L.; Li, Y.; Xu, S.; Lin, X.; Bai, Y. Lanthanide Bimetallic Mof-Based Fluorescent Sensor for Sensitive and Visual Detection of Sulfamerazine and Malachite. *Food Chem.* **2023**, *410*, 135390. [CrossRef]

33. Kumar, S.; Bhogal, S.; Kaur, G.; Malik, A.K.; Aulakh, J.S. Turn-Off Fluorescent Magnetic Mn-Zns Molecularly Imprinted Probe for the Detection of Chlorpyrifos in Vegetable Samples. *Spectrochim. Acta Part A Mol. Biomol. Spectrosc.* **2025**, *330*, 125623. [CrossRef]
34. El-Akaad, S.; Mohamed, M.A.; Abdelwahab, N.S.; Abdelaleem, E.A.; De Saeger, S.; Beloglazova, N. Capacitive Sensor Based on Molecularly Imprinted Polymers for Detection of the Insecticide Imidacloprid in Water. *Sci. Rep.* **2020**, *10*, 2045–2322. [CrossRef]
35. Kong, R.-M.; Ge, X.; Chen, J.; Dai, R.; Sun, F.; Zhao, Y.; Kong, W. Energy Transfer-Based Bimetallic Lanthanide Metal-Organic Frameworks for Ratiometric Fluorescence Detection of Anthrax Biomarker. *Microchem. J.* **2026**, *220*, 116588. [CrossRef]
36. Yan, Z.; Zhao, T.; He, X.; Pu, Y.; Zhu, D. Ratiometric Fluorescence Temperature Sensing of Dual-Lanthanide Mofs (Eu1-Xtbx-Btc) Prepared by Solvothermal Method. *Mater. Chem. Phys.* **2024**, *319*, 129379. [CrossRef]
37. Liu, B.; Chen, J.; Peng, Y.; Xiao, W.; Peng, Z.; Qiu, P. Graphitic-Phase C3n4 Nanosheets Combined with Mno2 Nanosheets for Sensitive Fluorescence Quenching Detection of Organophosphorus Pesticides. *J. Environ. Sci. Health Part B* **2022**, *57*, 441–449. [CrossRef]
38. Wahyudi, S.; Rizoputra, I.; Anas; Panatarani, C.; Bahtiar, A. Development of Novel Aptasensor Based Carbon Nano Dots (Cnds) with Fret Mechanism for Detection of Organophosphorus Pesticides. *Appl. Food Res.* **2025**, *5*, 101172. [CrossRef]
39. Li, H.; Yan, X.; Lu, G.; Su, X. Carbon Dot-Based Bioplatform for Dual Colorimetric and Fluorometric Sensing of Organophosphate Pesticides. *Sens. Actuators B Chem.* **2018**, *260*, 563–570. [CrossRef]
40. Gao, N.; Zhang, Y.; Huang, P.; Xiang, Z.; Wu, F.-Y.; Mao, L. Perturbing Tandem Energy Transfer in Luminescent Heterobinuclear Lanthanide Coordination Polymer Nanoparticles Enables Real-Time Monitoring of Release of the Anthrax Biomarker from Bacterial Spores. *Anal. Chem.* **2018**, *90*, 7004–7011. [CrossRef]
41. Wei, X.; Zhao, Y.; Zhang, H.; Jia, Q. Fluorescence sensor based on molecularly imprinted polymer and bimetallic Tb/Ce MOF for sensitive detection of thiamethoxam. *Spectrochim. Acta Part A Mol. Biomol. Spectrosc.* **2026**, *347*, 127005. [CrossRef]
42. Ghouri, Z.; Peng, S.; Wang, A.; Lian, Y.; Zhang, X.; Zeng, B.; Chen, Q.; Yang, H.; Li, J.; Li, L.; et al. Smartphone-based molecularly imprinted sensors for rapid detection of thiamethoxam residues and applications. *PLoS ONE* **2021**, *16*, e0258508. [CrossRef]
43. Rishabh; Rani, M.; Shanker, U. Fluorescence-based detection of thiamethoxam in agricultural and fruit samples by green synthesized N-CQDs from Citrus sinensis. *J. Food Compos. Anal.* **2025**, *139*, 107109. [CrossRef]
44. Zhang, C.; Ji, Y.; Zhang, Y.; Ye, B.; Zou, L. Facile One-Step Electrodeposition of Poly(L-Ornithine) Film on Glassy Carbon Electrodes for Sensitive Detection of Thiamethoxam. *J. Electrochem. Soc.* **2022**, *169*, 077508. [CrossRef]
45. Zhai, X.; Zhang, H.; Zhang, M.; Yang, X.; Gu, C.; Zhou, G.; Zhao, H.; Wang, Z.; Dong, A.; Wang, J. A rapid electrochemical monitoring platform for sensitive determination of thiamethoxam based on β–cyclodextrin-graphene composite. *Environ. Toxicol. Chem.* **2017**, *36*, 1991–1997. [CrossRef]
46. Xie, T.; Zhang, M.; Chen, P.; Zhao, H.; Yang, X.; Yao, L.; Zhang, H.; Dong, A.; Wang, J.; Wang, Z. A facile molecularly imprinted electrochemical sensor based on graphene: Application to the selective determination of thiamethoxam in grain. *RSC Adv.* **2017**, *7*, 38884–38894. [CrossRef]

Disclaimer/Publisher's Note: The statements, opinions and data contained in all publications are solely those of the individual author(s) and contributor(s) and not of MDPI and/or the editor(s). MDPI and/or the editor(s) disclaim responsibility for any injury to people or property resulting from any ideas, methods, instructions or products referred to in the content.